



EXPERIMENTAL CHARACTERIZATION OF MOMENT-ROTATION BEHAVIOR OF REINFORCED DISASSEMBLABLE MORTISE AND TENON JOINTS

Sanoop Siby¹, Aaron Münzer¹, Ric Zimmermann², Simon Aicher¹, Philippe Grönquist^{1,2}

ABSTRACT:

In the frame of sustainability, circular design, and modern robotic fabrication possibilities, traditional disassemblable Mortise-Tenon Joints (MTJs) using mostly only timber become increasingly interesting. However, in current European design practise, most traditional MTJs are still designed as full hinges, due to lack of precise knowledge about moment rotation behavior as well as weak performance of wood in compression perpendicular to the grain. This study analyses experimental moment rotation behavior of MTJs where the tenons were reinforced by splitting wedges, polymer concrete and screws, in order to maintain easy disassemblability. While initial moment-rotation stiffness was not significantly affected by the different reinforcement alternatives, the cyclic envelop and energy dissipation showed significant differences and potential to be tailored to engineered moment rotation behaviors.

KEYWORDS: mortise-tenon-joint, moment-rotation behavior, polymer concrete, cyclic testing, carpentry joints

1 – INTRODUCTION

Timber joints are fundamental for structural integrity, crucial for force transfer, member connections, and stability in multi-story buildings. In modern timber architecture, where sustainability and circular design are prioritized, joints support ecological objectives such as disassembly and reuse, extending material life cycles and promoting circular economy principles. Modern timber construction often relies on adhesives or mechanical fasteners for enhanced load-bearing capacity and rigidity, which undermines circularity by hindering reuse and disassembly. This limitation restricts the cascaded use of timber and its components and diminish their contribution to sustainability and post-building life cycle. Conversely, traditional carpentry joints, such as mortise and tenon joints (MTJs), are notable for their inherent simplicity and disassemblable nature. These fastener-free joints, used across cultures for centuries, rely on an interlocking mechanism to achieve structural resistance without adhesives or permanent fasteners. Historical applications, ranging from East Asian wooden frameworks to medieval European carpentry, demonstrate their versatility, durability, and resilience, especially in seismic performance [1–3]. Experimental studies e.g [4, 5] highlight their effective energy dissipation and ductility during cyclic loading, advantages for safety under seismic loads.

Despite these advantages, MTJs are underutilized in modern multi-story timber buildings due to insufficient load-bearing capacity, weak compression performance perpendicular to the grain, and the lack of comprehensive design guidelines [6]. Eurocode 5, for example, provides

some yet limited guidance on traditional joints, relegating their use and application in industry. Additionally, the labor-intensive production process of these joints also restricts their use. However, technological advancements in robotic fabrication and automated manufacturing are transforming this landscape. The recent advancements in robotic fabrication and automated manufacturing now allow for the precise and efficient production of these joints, fostering innovation and experimentation. This technological shift opens opportunities to revisit MTJs for both new construction and retrofitting of existing structures, such as medieval frameworks or solar panel integrations, while aligning with sustainability principles.

Despite the limitations, significant advancements have been made in understanding their mechanical performance and rotational behavior through experimental and theoretical studies. Key findings include the effect of connection gaps [4], the influence of compressive strength perpendicular to grain [7, 8], and the role of asperities on the microscopic scale in joint behavior [8, 9]. Finite element modeling (FEM) has further advanced the ability to simulate moment-resistance and deformation angle relationships [10, 11], providing accurate insights into their performance under static and cyclic loading conditions. Additionally, the impact of joint geometry on shear force resistance can be seen in [12, 13]. More recent research demonstrates the influence of combined shear and bending forces on rotational behavior, which extends beyond earlier models based purely on bending moments [14]. A Mortise-Tenon Joint (MTJ) shows two diagonally opposite contact zones (contact zones (CZS)) I and II during downward movement (positive rotation) of the tenon with respect to the mortise as depicted in Figure 1. The study [14] defined R_b as total compression force at the tenon bottom and the correspond-

¹Materials Testing Institute (MPA), University of Stuttgart, Germany, sanoopsiby@mpa.uni-stuttgart.de

²Institute of Construction Materials (IWB), University of Stuttgart, Germany, philippe.groenquist@iwib.uni-stuttgart.de

ing horizontal friction force is $f_b = \mu R_b$. Similarly R_t and $f_t = \mu R_t$ are the compressive and horizontal frictional forces on the top face of the tenon.

The present study investigates the reinforcement of the tenon at critical locations susceptible to compression failure perpendicular to the grain and CZS areas subjected to high stress, as illustrated in Figure 1. The focus is on mortise and tenon joints (MTJs), addressing their inherent limitations while maintaining the principles of disassemblability and reusability. Specifically, the study examines the impact of reinforcing the tenon in MTJs to mitigate challenges such as compression failure perpendicular to the grain, while ensuring the joint's ecological viability. This study builds upon the design, development, and fabrication of MTJs, as initially investigated in [15] including wedge penetrated reinforced tenon joints serving as benchmark here. It extends the previous work by conducting two additional reinforcement trials, which aimed to address key behavioral characteristics and failure modes identified through both static and cyclic loading tests. In addition to the geometry-based locking mechanism by wedge-penetrated reinforcement, which involves penetrating the tenon with a wedge, as traditionally employed in Japanese MTJs, two further reinforcement methods were explored: (2) a standardized local reinforcement of the tenon using self-tapping metal screws in alignment with European design guidelines, and (3) reinforcement using a filler material, namely polymer concrete offering enhanced bonding properties and improved resistance to compression. The performance of these reinforced specimens was compared to that of Unreinforced Mortise-Tenon Joint (UNR-MTJ) in [15] under cyclic loading to investigate the effects of tenon reinforcement on mechanical behavior of tenon-mortise connections. The hysteresis stiffness, ductility, stiffness degradation, and energy dissipation of these joints were analyzed in this study.

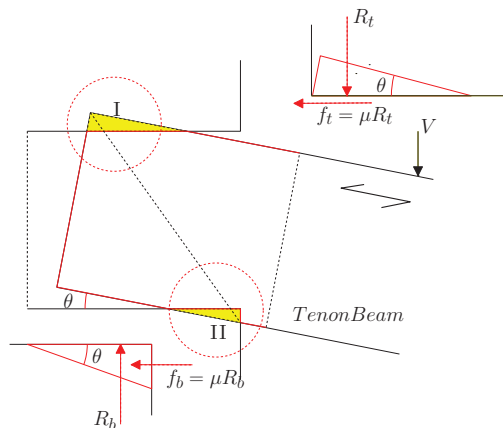


Figure 1: Mortise-tenon CZS located diagonally opposite at vertical positive loading (V) inducing a positive rotation (θ). Also shown are resultant reaction forces at the bottom (R_b) and top (R_t), accompanied by frictional forces (f_b and f_t)

2 – MATERIALS AND METHODS

2.1 BEAM AND COLUMN MATERIAL

Glued laminated timber (GLT) made from softwood specifically European spruce (*Picea abies*) according to EN

14080 [16] of strength class GLT 24c was used. The timber was provided by Hasslacher Norica Timber Industry which also performed the manufacture (milling) of the specimens using an in-house CNC joinery machine. GL24c is characterized by below given strength and stiffness properties. Characteristic bending strength $f_{m,g,k} = 24 \text{ N/mm}^2$, tensile strength $f_{t,0,g,k} = 17 \text{ N/mm}^2$ and shear strength $f_{v,g,k}$ of 2.5 N/mm^2 . Mean modulus of elasticity is $\rho_{gmean} = 11000 \text{ kg/m}^3$ and characteristic and mean density are 365 kg/m^3 and 400 kg/m^3 respectively. The moisture content (MC) of the specimens was measured using an electric moisture meter at two different locations per specimen for both tenon beam and mortise column. Average moisture contents for beams and columns were 11.4% and 10.9% respectively.

2.2 UNREINFORCED MORTISE TENON JOINT - DESIGN

The design and dimensional specifications of the UNR-MTJ were established during preliminary investigations conducted by [15]. The structural configuration and load considerations are based on a hypothetical two-story building designed with GLT beams and columns, supporting square floor bays of span 6.25 m. The UNR-MTJ was designed for vertical loads acting on the beam only, considering a design line-load of $q_d = 12.50 \text{ kN/m}$. The geometry and dimensions of the experimentally investigated configurations are depicted in Figure 2, which illustrates both the tenon-beam, Figure 2.a and mortise column, Figure 2.b. The tenon-beam is 1000 mm long, including a 200 mm protruding tenon matching the column width. The tenon length 200 mm ensures a snug fit within the mortise cavity. The beam has a cross-section depth of 360 mm, with a width matching the column's side length. The forces within the beam cross-section are transmitted to the column through a reduced section of 100 mm, equal to the tenon width. The mortise-column has a square cross-section with a 200 mm side length and a total height of 1400 mm. The mortise cavity is positioned 538 mm from the bottom and its dimensions are offset by 1 mm relative to the tenon dimensions, ensuring easy insertion. All contact edges are rounded by 10 mm to mitigate stress concentrations due to the geometry, as shown in Figure 2.

Two sets of configurations of UNR-MTJ, A and B were evaluated in the investigation by [15]; configuration A is characterized by the tenon being positioned at the bottom of the mortise as depicted in Figure 2. In contrast, configuration B represents an inverted setup, resulting in the tenon being positioned at the top of the mortise. Given, cyclic nature of the loading in testing both configurations are inherently the same. Therefore, this study utilizes exclusively configuration A.

2.3 REINFORCEMENT TYPES

The primary failure modes observed in initial test configuration (see Figure 6) of UNR-MTJ were of serviceability nature firstly due to excessive pullout of the tenon from the mortise, and finally material failure due to lateral compression failure of the tenon. This implied that the tenon was subjected to lateral loading at both ends, leading to crushing of the fibers at these locations due to geometrical

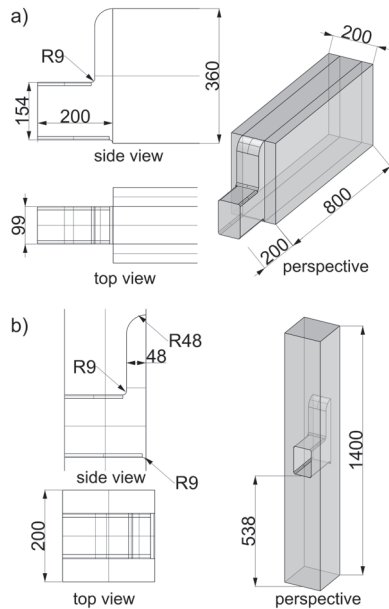


Figure 2: Specimen dimensions (in mm), with all corners rounded to a radius of $R = 9$ mm; a) tenon dimensions: The tenon-beam is 1000 mm long and 200 mm wide. The tenon itself measures 200 mm in length, 154 mm in depth, and 99 mm in width; b) mortise dimensions: The mortise-column is 1400 mm long, with the mortise insertion cavity positioned 538 mm from the bottom. The cavity dimensions are offset by 1 mm relative to the tenon dimensions to facilitate easy tenon insertion.

changes, which in turn resulted in the tenon slipping out during subsequent loading cycles.

Three reinforcement methods were investigated in this study: 1) Insertion of wedges to form a Wedge Penetrated Mortise-Tenon Joint (WP-MTJ), as traditionally employed in Japanese MTJs [17]. This method aims to mitigate excessive tenon pullout by geometrically locking the tenon inside the mortise through shape modification induced by the driven wedge, as illustrated in Figure 3. To enhance the lateral compression strength of the tenon and mitigate compression failure, two additional reinforcement strategies were examined: 2) a standardized local reinforcement method utilizing self-tapping metal screws, aligned with Eurocode 5 [18] design guidelines, referred to as Self Tapping Screw Reinforced Mortise-Tenon Joint (STR-MTJ), and 3) reinforcement using a polymer concrete filler material with improved bonding and compression resistance, Polymer Concrete Reinforced Mortise-Tenon Joint (PCR-MTJ). These reinforcement techniques were systematically tested to assess their influence on the mechanical performance of the UNR-MTJ.

2.3.1 Wedge Penetrated MT Joint Design

Referred to as WP-MTJ in this paper, this joint layout involves driving tropical hardwood wedges into pre-sawn slots in the tenon, leading to an increase in both dimension and material volume at the outer end of the tenon. This geometrical locking mechanism reinforces the MTJ and mitigates the risk of tenon pullout—a technique traditionally

employed in earthquake-prone regions such as Japan [17]. The driven-in wedges expand the tenon's cross-section, effectively tightening and pre-stressing the wood fibers inside the mortise. To accommodate these geometric change of the tenon due to the wedges, the mortise dimensions were adjusted accordingly. The smaller mortise opening on the side where the wedges were driven was enlarged and deepened, increasing the mortise opening depth from 155 mm to 175 mm. Beyond forming a frictional and positive locking mechanism between the tenon and mortise, this method also introduces additional stiffening material into the tenon section, effectively eliminating potential gaps. It was experimentally investigated in [15] to which extent wedges need to be driven by a wooden mallet, considering wedge indentation effects that result in tenon widening by 2 cm, or 10 mm on each side. The driving angle varied between 5° and 7° . The tests further evaluated splitting behavior along the tenon fibers and the efficiency of the locking mechanism achieved through wedge insertion.

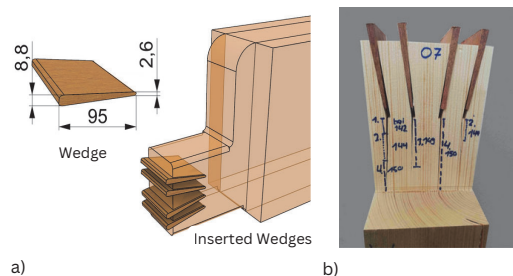


Figure 3: Hardwood wedge and WP-MTJ design; a) dimensions of the wedge with an isometric view of its insertion into the tenon; b) preliminary analysis of optimal insertion depth and angle.

The final wedges were inserted in pairs at an angle of 5° and depth of 60 mm as these parameters created least splitting while engaging maximum wood fibers as seen in Figure 3. The use of two wedge pairs resulted in improved stress distribution and lower stress peaks in the material, reducing the likelihood of splitting, as observed in experimental tests consequently, holding the tenon securely in place, preventing slippage and ensuring early activation of the joint under loading conditions.

2.3.2 Screw Reinforced Tenon Design

Self-tapping screws or fully threaded screws is a widely used method to locally reinforce wood against compression perpendicular to grain, particularly in load introduction areas, such as beam supports [19]. This is extensively covered in *prEN 1995-1-1:2025 (E)* [20] chapter 8.1.6.2. The relevant code reinforcement equation according for the combined timber and screw effects reads as Eq.(1).

$$F_{c,90,Rk} = \min \left\{ \begin{aligned} &k_{mat} b_{c,90} l_{1,ef} \cdot f_{c,90,k} + n \min\{F_{w,k}; F_{c,k}\}, \\ &bl_{2,ef} \cdot f_{c,90,k} \end{aligned} \right\} \quad (1)$$

The Eq.(1) gives the reinforcement capacity $F_{c,90,Rk}$ which determined by the minimum value between two expressions, considering material behavior, load application, and screw resistance. The factor k_{mat} accounts for material properties, such as stiffness in glulam. $b_{c,90}$ and $l_{1,ef}$ define the width and effective length of the load application area, while $f_{c,90,k}$ represents characteristic compression strength perpendicular to the grain. The reinforcement includes n screws, contributing their pull-out resistance $F_{w,k}$ or axial resistance $F_{c,k}$. The total width b and effective length $l_{2,ef}$ influence load distribution. As the tenon undergoes cyclic loading, the CZS regions at the top and bottom experience cyclic stresses too. This results in compressive forces acting on both surfaces of the tenon. To address this, overlapping reinforcement was applied at the top and bottom, in accordance with [20], section 8.1.6.2,(12). The equation provided in *prEN 1995-1-1:2025 (E)* [20] for support conditions applies when the supporting surface is composed of a material with high rigidity, such as steel. In such cases, fully threaded screws do not indent into the support, ensuring sufficient rotational capacity for uniform stress distribution. However, this condition does not reflect the loading experienced by the tenon, as illustrated in Figures 1.

Considering an unhindered rotation, the maximum length of the triangular CZS area can be considered as half the total tenon length ℓ_t . Hence Eq.(1) was solved for n (number of screws) employing, $\ell_{1,2,ef} = \ell_t/2$, to achieve a compressive resistance of twice the magnitude of the compressive resistance of reinforced tenon area of length $\ell_t/2$. The reinforcement of the tenon was carried out by two rows of four 6 mm diameter WÜRTH ASSY®plus VG 4 CSMP screws,(Product No. 0150106100) with a length of 100 mm. Additionally, reinforcement against tension perpendicular to grain close to the tenon notch was realized by means of three fully threaded WÜRTH ASSY®plus VG 4 CSMP, (Product No. 0150106100), each with diameter of 8 mm and length 300 mm. Both screw reinforcements were following the design recommendations of ETA-11/0190 [21]. This reinforcement as shown in Figure 4d was implemented to mitigate the risk of tensile perpendicular cracks which initiate at the tenon corner in-case of larger tenon rotations.

The designated reinforcement locations were pre-drilled using a 4.5 mm diameter drill hole for tenon reinforcement screws and a 6 mm diameter drill hole for tension-perpendicular screws. The drill depth corresponded to the length of each designated screw to ensure proper insertion. Edge distances and spacings are shown in Figure 4 and quantified in Table 1. The realized spacings a_1 and a_2 as well as edge distances $a_{4,c}$ perpendicular to grain to grain were throughout larger as compared to the minimum values specified in [20]. However edge distance $a_{3,c}$ parallel to grain was much smaller than the code - prescription (Table 1) in order to effectively reinforce the highly compressed bearing area within the CZS regions.

2.3.3 Polymer Concrete Reinforced Tenon Design

Just as self tapping screws, an emerging reinforcement technique for timber components under compression per-

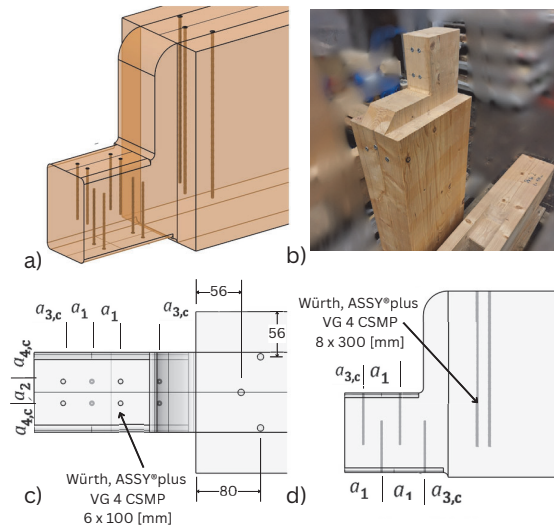


Figure 4: STR-MTJ reinforcement placement and design; a) Isometric view of overlapping screw reinforcement at the tenon's top and bottom, along with tension-perpendicular screws; b) fabricated tenon with screw reinforcement; c) top view showing compression-perpendicular screws and clear spacing notations; d) section view illustrating screw reinforcement with normative spacing.

Table 1: Norm recommended and provided values for edge and clear spacings

	a_1	a_2	$a_{4,c}$	$a_{3,c}$
prEN 1995-1-1	30	15	12	60
provided	36	27	36	36

pendicular to grain involves the application of polymer concrete [22]. In the study by [22], polymer concrete was utilized to reinforce the compression support zone of a modified glulam beam via drilled holes filled with polymer concrete. This lead to an increased stiffness and compressive strength at the support area according to study. Further studies, such as [23], claim that polymer concrete infill was able to achieve a load increase of 284 % compared to 225 % for self-drilling screws using push-out tests with glulam blocks.

Building on this research, the third reinforcement method explored in this study, denoted as PCR-MTJ, involved the use of polymer concrete infills to enhance compression perpendicular to grain resistance in the tenons. The initial investigations by [24] provides insights, having numerically and experimentally examined perpendicular to grain push-out tests on cylindrical polymer concrete infills in Glulam and CLT blocks. The investigation also examined failure modes at the interface between polymer concrete and wood, with a focus on bond strength, edge distance influence, geometric edge conditions. Further a reinforcement design was proposed for cylindrical polymer concrete infills in timber loaded under compression perpendicular to grain. Four different failure modes were observed when loading polymer concrete reinforced infills namely, a) failure of adhesive joint, b) Failure of wood in rolling thrust c)

failure of wood in transverse tension and d) failure of polymer concrete infill. The investigation revealed that stress concentrations at the adhesive joint depend on diameter and height of the infill. The proposed design principles closely resemble the reinforcement mechanisms of self-tapping screws, as defined in [20]. In the investigation, the maximum characteristic load-bearing capacity ($F_{c,90,Rk,pc}$) is determined by two failure mechanisms: (i) adhesive bond failure between polymer concrete and wood, represented by the first term in Eq.(2) and (ii) failure of the polymer concrete infill itself, represented by the second term of Eq.(2).

$$F_{c,90,Rk,pc} = \min(f_v \cdot A_{contact,pc}, f_{c,pc,k} \cdot A_{infill,pc}) \quad (2)$$

The equation defines the minimum value between two terms: the product of the characteristic bond strength of the adhesive joint, f_v , and the surface area of the cylindrical infill, $A_{contact,pc}$; and the product of the characteristic compressive strength of polymer concrete, $f_{c,pc,k}$, and the cross-sectional area of the infill, $A_{infill,pc}$. According to [24], given an infill diameter (d_{pc}) and bonded height (h_{pc}), the respective contact surface area and cross-section area are calculated as $A_{contact,pc} = \pi \cdot d_{pc} \cdot h_{pc}$ and $A_{infill,pc} = \pi d_{pc}^2/4$. The experimental investigation provided a mean bond strength (\pm standard deviation) of $f_{v,exp,mean} = 6.45 \pm 1.83 \text{ N/mm}^2$. The rather high scatter, denoted by the a coefficient of variation (COV) of 29% results from complex interaction effects on . To prevent polymer concrete infill failure, the minimum required diameter ($d_{pc,min}$) is determined by Eq.(3), as the resistance to failure of polymer concrete infill must be greater than resistance of the adhesive joint .

$$d_{pc,min} \geq 4 \cdot \frac{h_{pc} \cdot f_{v,k}}{f_{c,0,pc,k}} \quad (3)$$

Considering rolling shear resistance, the investigation recommends minimum spacing and edge distances for infills. To avoid rolling shear failure the minimum spacing between the axes of adjacent polymer infills as well as edge distance of an infill to the end grain face is obtained by equating areas, $A_{contact,pc}$ to $A_{rolling,shear} = e_{1,2} h_{pc}$ resulting in

$$e_1 \geq 0.8 \cdot \pi \cdot d_{pc} \cdot \frac{h_{pc}}{h_{sample}} \quad (4)$$

$$e_2 \geq 0.7 \cdot \pi \cdot d_{pc} \cdot \frac{h_{pc}}{h_{sample}} \quad (5)$$

The difference between e_1 and e_2 is bound to empirical observations. Following these design recommendations, two 20 mm diameter polymer concrete infills were placed along the tenon's mid-width, with a center-to-center spacing of $e_1 = 90 \text{ mm}$, as illustrated in Figure 5.

The material specifications of the utilized polymer concrete are provided in Table 2. The holes with 20 mm diameter were drilled at the design tenon locations, and polymer concrete was mixed and poured within an half-hour after drilling. To optimize bonding and stress distribution, a rectangular groove was added atop of the tenon, to form

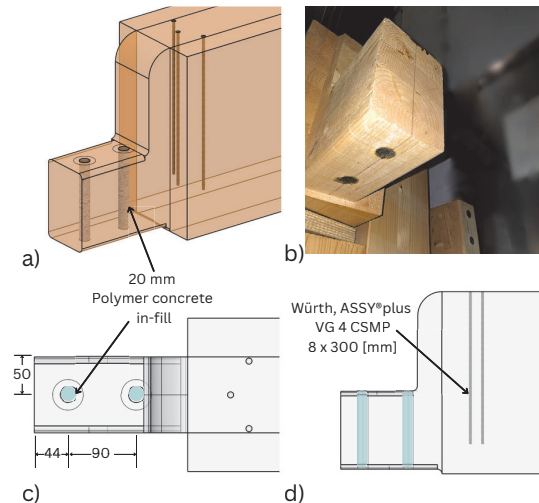


Figure 5: PCR-MTJ reinforcement placement and design; a) Isometric view illustrating polymer tenon concrete infill and reinforcement screws; b) fabricated tenon with polymer concrete infill; c) top view of reinforcement and spacing; d) section view.

Table 2: Technical properties of the polymer concrete tested

Property	Value
Density	approx. 2.0 g/cm ³
Compressive strength	>100 N/mm ²
Bending strength	>35 N/mm ²
E-modulus (static)	14000 N/mm ²
Maximum grain size	1.6 mm
Mixing ratio	A:B:C = 3.04:0.78:21.18 (parts by weight)
Processing time	approx. 2.5 - 4 hours at 23°C
Processing temperature	15 - 25 °C
Curing	approx. 24 hours

a 5 mm deep and 20 mm wide channel connecting both infills. A metal plate was placed at the tenon cavity bottom and polymer concrete was filled in stage-wise compaction to ensure void-free filling. Once the cavity was completely filled, an additional plate was positioned on the top of the tenon, and both plates were securely clamped to maintain pressure and improve adhesive penetration. The specimens were left to cure for 28 days to ensure complete polymer concrete binding with the tenon fibers. The manufactured polymer concrete reinforced tenon can be seen in Figure 5b.

2.4 EXPERIMENTAL TESTING PROTOCOL

The tenon beam was horizontally pre-inserted into the mortise column, as depicted in the test setup shown in Figure 6. The load was applied using specially hinged swing frame, which was clamped to the tenon as shown in Figure 6a. To counteract uplifting of the column during upward bending, the column was clamped as shown in Figure 6b. Mortise column was rigidly fixed and supported using a rigid steel truss to ensure structural stability. Clamps were strategically employed to mitigate any lateral displacement.

Figure 6c further depicts the pin mounted to the load-

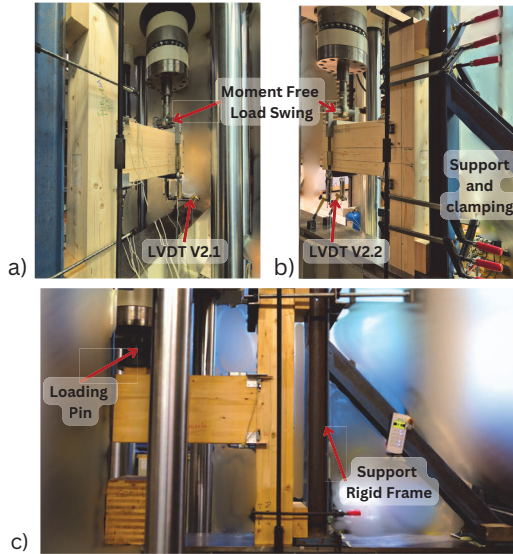


Figure 6: Test set-up; a) back side; b) front side; c) downward loading test, front side

ing piston in scenarios requiring large displacements. The swing was omitted in such cases due to significant deformation of the swing frame. The remaining two transducers, labeled “V”, with a maximum range of 100 mm, were installed to measure the vertical displacements at the cantilever end, both on the front and rear faces of the beam. Displacement and load data were directly recorded in real-time from the loading machine, complemented by the displacement data obtained from the externally mounted LVDTs used for rotation determination.

The clear distance, corresponding to the lever arm distance from the center of the loading piston to the start of the joint, was fixed at 0.65 m in all tests. Prior to loading, the tenon was fully inserted into the mortise with no visible gaps to ensure proper joint contact. The testing procedure guidelines outlined in [25] was modified to a displacement-controlled protocol with four specified amplitudes: ± 10 mm, ± 20 mm, ± 40 mm, and ± 60 mm, were conducted, each with three number of cycles. Although [25] prescribes loading speeds within the range of 0.02 mm/min to 0.2 mm/min, the tests were executed at a higher loading speed of 5 mm/min for both upward and downward displacement, to investigate the joint behavior under much faster loading conditions. Failure of the test specimen was defined either by loss of bearing capacity or slide-out failure, occurring when the tenon experienced a horizontal pullout of 45 mm relative to the mortise.

At high vertical displacement of the cantilever, the loading swing proved unsuitable, inducing unintended horizontal forces, leading to deformation, load inaccuracies, and hazardous conditions. Since the testing apparatus was designed primarily for vertical force application, excessive deformation of the swing frame necessitated corrective measures. In these cases, such as 80 mm displacement for STR-MTJ, the loading swing was replaced by a pin, allowing precise vertical force application without biasing lateral effects. Figure 6c illustrates this modification,

showing the downward loading pin in scenarios with large displacements. The experimental results were analyzed in accordance with [25], focusing on yield points, energy dissipation, and ductility characteristics under cyclic loading.

3 – RESULTS AND DISCUSSION

3.1 HYSTERETIC AND MOMENT-ROTATION CURVES

The bending moment M and its corresponding rotation of the joint θ are determined as follows:

$$M = PH, \quad \theta = \frac{\Delta}{H} \quad (6)$$

where P is the load applied by the actuator, H is the lever arm which is the horizontal distance between loading point and vertical face of the column and Δ is the vertical load displacement measured at the loading point.

Figure 7 shows the hysteresis and envelop curves of the three reinforced MTJs. The hysteresis curves of the STR-MTJ and PCR-MTJ shown in Figure 7a and Figure 7b respectively show a similar trend. At start of loading, due to the low engagement - bound to the small CZS and a significant gap between the tenon and mortise, the slopes of the hysteresis curves very small. As the rotation increases, the rotation stiffness grew rapidly with PCR-MTJ showing a higher engagement at initial 10 mm displacement than STR-MTJ. The curves show a pronounced moment-rotation asymmetry, where the positive downward loading curves reveal a higher stiffness than the upward negative loading curves. This results from the different constraints under positive and negative loading cycles as the MTJ moment in configuration A (defined in section 2.2), where the tenon is placed lower leading to push-out and the loosening of the tenon under negative loading. Displacements between 50 mm to 60 mm were exclusively achieved in the downward direction due to the limitations of load swing and the pull out of tenon as mentioned earlier. Hence, the large rotation at the cantilever end where significant slip can be observed in Figure 7a and Figure 7b exists only for positive downward loading in STR-MTJ. The significant slip and the reduced stiffness in load bearing capacity is due to the tenon being significantly displaced inside the mortise rather than an observed ultimate material failure. In case of WP-MTJ as shown in Figure 7c the wedges were gradually pushed out at increased loading and the test was halted when the tenon was laterally pushed out beyond the specified protocol limit. The colored solid thick line on each plot represents the envelop curve, joining the peak bending capacity achieved in each cycle.

Figure 8 shows the envelope curves of all reinforcement cases overlapped for comparison. As can be seen clearly the un-reinforced MTJ starts to yield at around $\theta = 0.035$ rad, whilst all reinforced tenons maintain load bearing capacity.

3.2 LOAD-CARRYING CAPACITY AND FAILURE MODES

In view of the hysteresis loading cycles shown in Figure 7, the peak load achieved by each reinforced MTJ at maximum displacement amplitudes are provided in table 3.

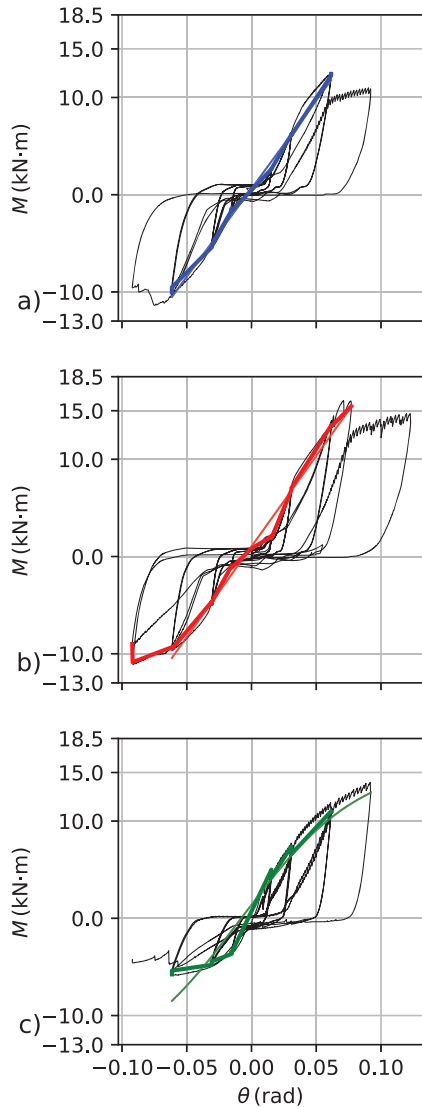


Figure 7: Hysteresis and envelope curves depicting the moment-rotation behavior of different reinforced MTJ; a) PCR-MTJ; b) STR-MTJ; c) WP-MTJ

At initial displacement of ± 10 mm, wedge-reinforced specimens exhibited 1.9% more load carrying capacity as compared to PCR-MTJ and about 2.6% more as compared to STR-MTJ in peak load values. This indicates significant contact and transfer of forces due to engagement of areas in the CZS zones of the MTJ and closure of any gaps. On initial positive downward displacement, WP-MTJ demonstrated significant activation, while both PCR-MTJ and STR-MTJ activated only after 5 mm, as recorded in the experimental data. The lower activation of STR-MTJ may be attributed to absence of stiff material at contact zone (CZS)-I, where PCR-MTJ had the polymer concrete rectangular channel, enhancing early load resistance. As the downward displacement amplitude increased the load bearing capacity of all reinforced MTJs started to align and be activated simultaneously, with WP-MTJ still ahead by approximately 1.5 kN ahead of other reinforced MTJs. Even at 20 mm

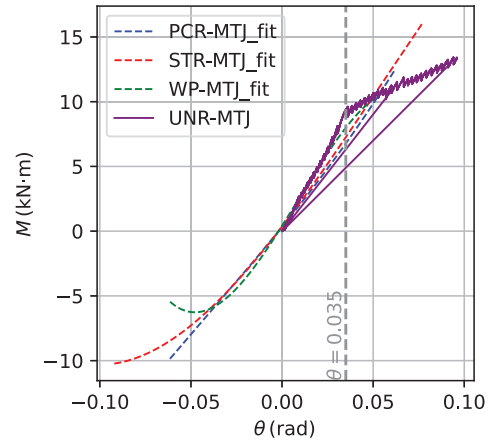


Figure 8: Envelope curves depicting the moment-rotation relationship for each Reinforced Mortise-Tenon Joint (R-MTJ), illustrating comparative moment capacity.

Table 3: Maximum loads per displacement cycle

Displacement	Wedge	Polymer Concrete	Screws
[mm]	[kN]	[kN]	[kN]
10	7.69	4.10	2.92
-10	-5.64	-2.59	-1.78
20	11.37	9.50	10.49
-20	-7.34	-8.34	-7.52
40	16.95	19.11	20.72
-40	-8.87	-15.43	-14.62
60	19.95	15.91	23.78*
-60	-6.66	14.50	-13.86

* test halted at 50 mm due to extensive load swing deformation.

downward displacement the STR-MTJ has already been activated, exhibiting peak loads slightly greater than PCR-MTJ. As the positive displacement increases to 40 mm, the PCR-MTJ and STR-MTJ maintained similar higher peak loads, while WP-MTJ peaked at significantly lower loads. As positive rotation displacement progressed the driven wedges were observed to be pushed out due to the small cross-section of the loaded fibers between the wedges and the mortise contact surface. At 60 mm positive displacement, the tenon had already been significantly pushed out from the flush surface by more than 10 mm leading to a lower area in the CZS. This may have contributed to the failure to achieve the higher stiffness that was easily reached during the 40 mm displacement cycle. The negative upward displacement cycles exhibited a trend similar to the positive displacement cycles, with lower peak loads. This difference is likely attributable to the asymmetric tenon design, resulting in uneven loading between the top and bottom surfaces of the tenon. After testing, the MTJs were disassembled to observe failure modes and damage induced to components. The distortion of the disassembled tenons of both STR-MTJ and PCR-MTJ post loading can be seen in Figure 9 and Figure 10. In both STR-MTJ and PCR-MTJ, a clear compression perpendicular indentation

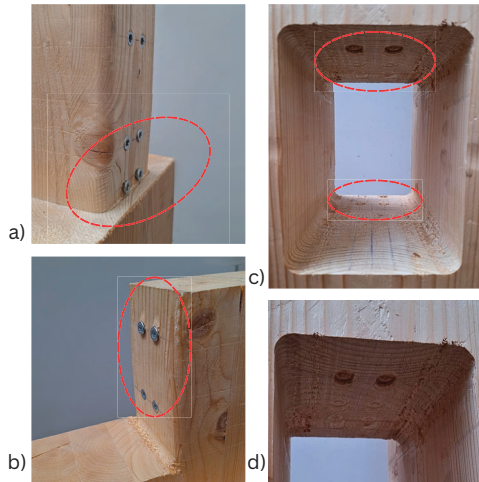


Figure 9: Disassembled screw reinforced MTJ post loading; a) tenon bottom; b) tenon top; c) mortise Interior; d) zoomed view

can be observed on the tenon at diagonally opposite CZS on the top and bottom of the tenon as stated in earlier in Figure 1. Figure 9a shows encircled in red the screws on the beam side of the Self Tapping Screw Reinforced Tenon (STR-T) which were initially flush with the surfaces but now protrude out due to excessive localized strain due to local compression. The same is evident in Figure 10a. In case of Polymer Concrete Reinforced Tenon (PCR-T) encircled in red marked by distinct seam indentation at approximately the same location. Figure 9b and Figure 10b shows the top faces of STR-T and PCR-T respectively. As observed on the bottom screws, screws which were flush with the surface located at the diagonally opposite top face of the tenon can be seen protruding out due to local deformation. In case of PCR-T, Figure 10b shows compression cracks on the polymer concrete channel connecting the two polymer concrete infill on the diagonally opposite top face of the tenon. In addition after local deformation of the tenon in

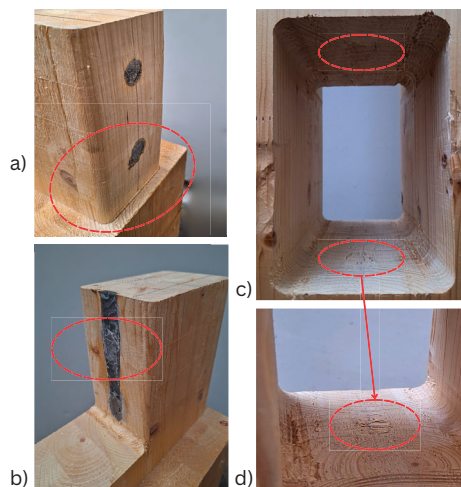


Figure 10: Disassembled polymer concrete reinforced MTJ post loading; a) tenon bottom; b) tenon top; c) mortise Interior; d) zoomed view

compression perpendicular to fiber the stiff reinforcement starts to locally punch into the interior mortise surface as evident from Figure 9c and Figure 10c. The significant push-out of the tenon resulted in the stiff reinforcement i.e. polymer concrete infill and self tapping screws to be gradually shifted and be directly near the exposed edge of the mortise, as seen in indentations in Figure 9d and Figure 10d. This may be the reason to observe increased slippage and failure at higher displacement amplitudes. Most often than not in case of PCR-MTJ and STR-MTJ, the test had to be terminated due to the limitations of the testing machine due to excessive deformation of the loading apparatus.

3.3 STIFFNESS, DUCTILITY, AND ENERGY DISSIPATION

Stiffness variation of the various tenon reinforced MTJ can be tracked along with the envelop curve by computing the secant stiffness K_i using Eq.(7). M_i is the peak bending moment at first cycle in the i th displacement amplitude and θ_i is the corresponding rotation angle of M_i .

$$K_i = \frac{|+M_i| + |-M_i|}{|+\theta_i| + |-\theta_i|} \quad (7)$$

The evolution of the stiffness of the different reinforcement types is portrayed in Figure 11, which shows K_i vs δ which is the maximum deformation amplitude in mm. As mentioned before in the load bearing section 3.2, the WP-MTJ benefits from prestressed wood fibers and improved engagement, while the PCR-MTJ exhibited stiffness enhancements due to the existence of a polymer concrete channel at the CZS. Demonstrated by the higher stiffness of WP-MTJ, followed by PCR-MTJ. At initial small displacements or rotations, WP-MTJ exceeded PCR-MTJ by 1.8% and STR-MTJ by 2.7%. As rotations/displacement increase, the WP-MTJ exhibited a gradual decrease in stiffness due to wedge expulsion, while the STR-MTJ and PCR-MTJ showed increasing stiffness, gradually becoming comparable with each other. This behavior was attributed to compressive forces initiating at the extreme CZS of the tenon and moving inward during loading. With further loading, the STR-MTJ surpassed both the PCR-MTJ and WP-MTJ in rotational stiffness. The stiffness of the WP-MTJ became lower than that of the PCR-MTJ at the last test with a displacement of 60 mm, with STR-MTJ maintaining higher stiffness compared to the rest of the reinforced MTJs.

The energy dissipation of each of the connections was determined in accordance to [25] using the envelop as illustrated in Figure 8. Elastic potential energy, E_p represents the energy stored in a system during the elastic recoverable deformation phase and energy dissipation, E_d corresponds to the total energy irreversibly lost during a loading-unloading cycle. Together, the values of E_d, E_p were calculated at peak load and the equivalent damping ratio v_{eq} defined as $v_{eq} = E_d/(2\pi E_p)$ provide essential insights into the energy absorption and damping efficiency of the mortise and tenon joint configurations analyzed under cyclic loading conditions.

The results presented in Table 4 demonstrate that each mortise and tenon joint (MTJ) type exhibits distinct energy

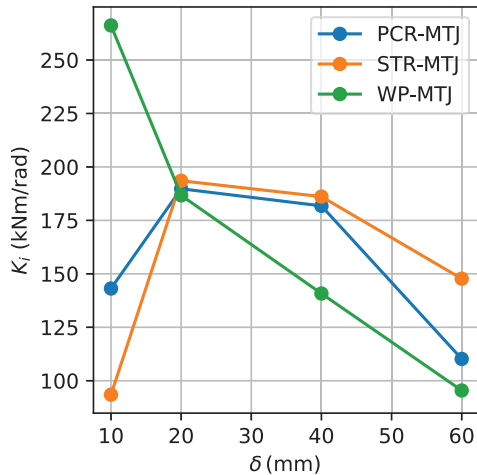


Figure 11: Stiffness trend curves illustrating variations in rotational stiffness for different reinforced MTJ

Table 4: Energy dissipation and damping measure

MTJ Type	E_d (J)	E_p (J)	ν_{eq} (-)
PCR-MTJ	899.88	351.09	0.40
STR-MTJ	1193.96	609.6	0.31
WP-MTJ	736.25	740.76	0.158

dissipation and damping characteristics, reflecting their different mechanical performance under cyclic loading. The STR-MTJ displayed the highest energy dissipation, indicating increased capacity for energy absorption through inelastic deformation and damping mechanisms. The WP-MTJ follows STR-MTJ, while the PCR-MTJ exhibited the lowest dissipation. The WP-MTJ demonstrated the highest recoverable elastic potential energy, highlighting its greater capacity to store energy during elastic deformation. The PCR-MTJ achieved the highest damping ratio, suggesting its enhanced capacity to dissipate energy at reversed loading situations. The STR-MTJ followed closely, while the WP-MTJ displayed the lowest damping ratio. The higher damping ratio of the PCR-MTJ suggests its effectiveness in reducing vibration amplitudes. However, the higher energy dissipation observed in the STR-MTJ highlights its robustness under cyclic loading conditions. Meanwhile, the WP-MTJ is better for elastic energy storage, making it a favorable candidate for applications requiring recoverable energy and structural resilience, but its lower dissipation and damping ratio might limit its effectiveness in scenarios requiring significant energy absorption. In traditional timber joints, such as those studied in [1], performance evaluations of joints retrofitted with Near Surface Mounted (NSM) steel rods and Glass Fibre Reinforced Polymers (GFRP) sheets show cumulative energy dissipation values comparable to this study for a maximum displacement of 35 mm, with NSM reinforcements exhibiting much lower values. In [3], energy dissipation of different traditional Fork-Column Dou-Gong specimens was measured as approximately 400 J for an end rotation angle of $\theta = 0.10$, which is also lower than the values obtained in this study.

Findings in [8] on the cyclic behavior of ancient Chinese wooden frames with mortise–tenon joints indicate that for a maximum vertical displacement of 60 mm, the energy dissipation is only around 200 J, below the levels achieved in all specimens examined here, despite being specifically designed for vertical displacement only. These values highlight the hidden potential benefit of such joints in terms of design for resistance to horizontal loads using ductility and energy dissipation.

4 – CONCLUSION

This study demonstrated that reinforcement techniques such as self-tapping screws, polymer concrete, and wedges enhance the structural performance of MTJs, improving bending moment capacity, stiffness, and ductility. In contrast, UNR-MTJ yielded earlier, at a low rotation angle of 0.035 rad, emphasizing the potential of reinforcement. The investigated reinforcement alternatives of MTJs portrayed different behaviors in terms of load bearing capacity, rotation stiffness and energy dissipation characteristics emphasizing their potential to tailor joint performance in according structural requirements.

Reinforcement methods that maximize contact area and prevent localized indentation lead to improved performance on MTJs. Stiffer materials at critical zones improved initial stiffness and engagement at low rotations (as seen in PCR-MTJ and WP-MTJ). At higher displacements, embedded reinforcing materials in the tenon section (as seen in PCR-MTJ and STR-MTJ) showed better structural behavior, while localized compressive strain perpendicular to the grain facilitated tenon sliding. To mitigate this, reinforcement strategies should prioritize strain reduction, particularly at the CZS. Additionally, lateral tenon pullout must be controlled to ensure full engagement. Experimental limitations restricted load observations beyond a vertical displacement of 60 mm displacement, warranting improvements in the test setup. Energy dissipation capacity varied across reinforcement types, highlighting the need of future research on optimizing reinforcement strategies to improve structural resilience, mitigate sliding effects. The determination of ultimate capacities necessitates an improved loading set-up.

5 – ACKNOWLEDGMENT

The authors sincerely thank Juan Patricio Lara Ditzel for his support, expertise, and valuable discussions. Adrian Niehörster and HASSLACHER Holzbauteile GmbH & Co. KG are acknowledged for their generous support with material and manufacturing. This research was financially supported by the Deutsche Forschungsgemeinschaft (DFG, German Research Foundation) under Germany’s Excellence Strategy – EXC 2120/1 – 390831618.

REFERENCES

- [1] E. Poletti, G. Vasconcelos, J. M. Branco, and A. M. Koukouviki. “Performance evaluation of traditional timber joints under cyclic loading and their influence on the seismic response of timber frame structures.” In: *Construction and Building Materials* 127 (2016), pp. 321–334.

- [2] X. Li, J. Zhao, G. Ma, and W. Chen. “Experimental study on the seismic performance of a double-span traditional timber frame.” In: *Engineering Structures* 98 (2015), pp. 141–150.
- [3] Q. Xie, L. Wang, L. Zhang, W. Xiang, and W. Hu. “Rotational behaviors of fork-column dou-gong: experimental tests and hysteresis model.” In: *Journal of Performance of Constructed Facilities* 34.3 (2020), p. 04020032.
- [4] W.-S. Chang and M.-F. Hsu. “Rotational performance of traditional Nuki joints with gap II: the behavior of butted Nuki joint and its comparison with continuous Nuki joint.” In: *Journal of Wood Science* 53 (2007), pp. 401–407.
- [5] D. F. D’Ayala and P. H. Tsai. “Seismic vulnerability of historic Dieh–Dou timber structures in Taiwan.” In: *Engineering structures* 30.8 (2008), pp. 2101–2113.
- [6] H. Salamaha, S. H. Lee, and T. H.-K. Kang. “Investigation of design methods in calculating the load-carrying capacity of mortise-tenon joint of timber structure.” In: *Department of Architecture and Architectural Engineering, Seoul National University* (2023). Received July 11, 2023; Revised September 25, 2023; Accepted September 25, 2023.
- [7] K. Ogawa, Y. Sasaki, and M. Yamasaki. “Theoretical estimation of the mechanical performance of traditional mortise–tenon joint involving a gap.” In: *Journal of Wood Science* 62 (2016), pp. 242–250.
- [8] Q. Xie, L. Zhang, S. Li, W. Zhou, and L. Wang. “Cyclic behavior of Chinese ancient wooden frame with mortise–tenon joints: friction constitutive model and finite element modelling.” In: *Journal of Wood Science* 64 (2018), pp. 40–51.
- [9] H. Jamshidi and H. Ahmadian. “A modified rough interface model considering shear and normal elastic deformation couplings.” In: *International Journal of Solids and Structures* 203 (2020), pp. 57–72.
- [10] Z. Guan, A. Kitamori, and K. Komatsu. “Experimental study and finite element modelling of Japanese “Nuki” joints—Part one: Initial stress states subjected to different wedge configurations.” In: *Engineering Structures* 30.7 (2008), pp. 2032–2040.
- [11] Z. Guan, A. Kitamori, and K. Komatsu. “Experimental study and finite element modelling of Japanese “Nuki” joints—Part two: Racking resistance subjected to different wedge configurations.” In: *Engineering Structures* 30.7 (2008), pp. 2041–2049.
- [12] S. Okamoto, M. Nakatani, N. Akiyama, K. Tanaka, and T. Mori. “Verification of the shear performance of mortise and tenon joints with top and bottom notches at the beam end.” In: *Journal of Wood Science* 67 (2021), pp. 1–23.
- [13] M. Wang, X. Song, X. Gu, and J. Tang. “Bolted glulam beam-column connections under different combinations of shear and bending.” In: *Engineering Structures* 181 (2019), pp. 281–292.
- [14] Y.-J. Wu, L. Wang, H.-S. Lin, L.-P. Zhang, and Q.-F. Xie. “Effect of shear force on the rotational performance of straight mortise-tenon joints.” In: *Structures*. Vol. 41. Elsevier, 2022, pp. 501–510.
- [15] R. Zimmermann. “Japanese Carpentry Connections as Inspiration for Modern Earthquake-Resistant Multi-Storey Timber Buildings.” Received November 30, 2024. Master’s thesis. Institute of Construction Materials, Material Testing Institute, University of Stuttgart, 2024.
- [16] EN 14080. *Timber structures – Glued laminated timber and glued solid timber – Requirements*. Brussels, Belgium: European Committee for Standardization, 2013.
- [17] H. Sakata, Y. Yamazaki, and Y. Ohashi. “A study on moment resisting behavior of mortise-tenon joint with dowel or split wedge.” In: *15th World conference on earthquake engineering, Lisbon, Portugal*. 2012.
- [18] Eurocode 5. *Design of timber structures – Part 1-1: General and rules for buildings*. EN 1995-1-1. Brussels, Belgium: European Committee for Standardization, 2010.
- [19] P. Dietsch and A. Ringhofer. “Self-tapping Screws as Reinforcement for Structural Timber Elements.” In: *Reinforcement of Timber Elements in Existing Structures: State-of-the-Art Report of the RILEM TC 245-RTE*. Springer, 2021, pp. 7–27.
- [20] *prEN 1995-1-1:2025 (E)*. Draft European Standard. Work in progress, subject to change. CEN (European Committee for Standardization), 2025.
- [21] ETA-11/0190. *European Technical Assessment ETA-11/0190 of 23 July 2018*. Published by Deutsches Institut für Bautechnik. 2018.
- [22] M. Jahreis, M. Kästner, W. Hädicke, and K. Rautenstrauch. “Development of a high-performance hybrid system made of composites and timber (High-Tech Timber Beam®).” In: *Materials and Joints in Timber Structures: Recent Developments of Technology*. Springer. 2014, pp. 423–431.
- [23] W. Hädicke, M. Kästner, and K. Rautenstrauch. “Highly efficient strengthening of local load introduction areas of engineering wood structures using polymer concrete grouting.” In: *World Conference on Timber Engineering, proceedings of WCTE*. 2014.
- [24] P. K. Hochbein. “Experimental and Numerical Investigations of Reinforcements of the Load Application Areas in Glulam and CLT Components Using Polymer Concrete Grouting.” Received May 31, 2024. Master’s thesis. Institute of Construction Materials, Material Testing Institute, University of Stuttgart, 2024.
- [25] EN 12512:2001. *Timber Structures - Testing of Mechanical Fasteners*. Brussels, Belgium: CEN (European Committee for Standardization), 2001.